

Spin-strain interaction in nitrogen-vacancy centers in diamond

Péter Udvarhelyi,^{1,2} V. O. Shkolnikov,³ Adam Gali,^{2,4} Guido Burkard,³ and András Pályi^{5,6,*}

¹*Department of Biological Physics, Eötvös Loránd University, Pázmány Péter sétány 1/A, H-1117 Budapest, Hungary*

²*Wigner Research Centre for Physics, Hungarian Academy of Sciences, P.O. Box 49, H-1525, Budapest, Hungary*

³*Department of Physics, University of Konstanz, D-78457 Konstanz, Germany*

⁴*Department of Atomic Physics, Budapest University of Technology and Economics, Budafoki út 8., H-1111 Budapest, Hungary*

⁵*Department of Physics, Budapest University of Technology and Economics, Budafoki út 8., H-1111 Budapest, Hungary*

⁶*MTA-BME Exotic Quantum Phases “Momentum” Research Group, Budapest University of Technology and Economics, Budafoki út 8., H-1111 Budapest, Hungary*



(Received 7 December 2017; published 2 August 2018)

The interaction of solid-state electronic spins with deformations of their host crystal is an important ingredient in many experiments realizing quantum information processing schemes. Here, we theoretically characterize that interaction for a nitrogen-vacancy (NV) center in diamond. We derive the symmetry-allowed Hamiltonian describing the interaction between the ground-state spin-triplet electronic configuration and the local strain. We numerically calculate the six coupling-strength parameters of the Hamiltonian using density functional theory, and propose an experimental setup for measuring those coupling strengths. The importance of this interaction is highlighted by the fact that it enables to drive spin transitions, both magnetically allowed and forbidden, via mechanically or electrically driven spin resonance. This means that the ac magnetic field routinely used in a wide range of spin-resonance experiments with NV centers could in principle be replaced by ac strain or ac electric field, potentially offering lower power requirements, simplified device layouts, faster spin control, and local addressability of electronic spin qubits.

DOI: [10.1103/PhysRevB.98.075201](https://doi.org/10.1103/PhysRevB.98.075201)

I. INTRODUCTION

The nitrogen-vacancy (NV) color center consists of a nitrogen atom substituting a carbon atom adjacent to a vacancy in diamond (see Fig. 1). In the negatively charged state, it shows a broad fluorescence with zero-phonon line at 637 nm [1,2] and possesses a spin $S = 1$ ground state [3–6]. The electron spin of the NV center can be initialized, coherently manipulated, and read out in optically detected magnetic resonance (ODMR) experiments [7], even at the level of individual centers [8]. This electronic spin degree of freedom is robust even at room temperature, and its coherence time is typically a few microseconds in natural diamond [7], reaching milliseconds in ¹²C enriched diamonds [9]. Because of these favorable properties of the NV center, it provides a versatile and highly coherent platform for the experimental realization of many quantum information schemes. To maximize the potential of these defects for various quantum communication [10–12], quantum sensing [13–21], and quantum computing [22–24] applications, it is crucial to understand the interaction of the center’s electronic system with its environment, most notably externally induced electromagnetic fields, and deformations of the crystal lattice.

In this work, we provide a theoretical description of the latter, i.e., the *spin-strain interaction Hamiltonian* of the spin-triplet ground-state electronic configuration of the negatively charged NV defect. Even though in recent years this interaction has been studied intensively [19–21,25–37], to our knowledge

the correct and complete form of the interaction Hamiltonian of the ground-state spin-1 vector \mathbf{S} and the 3×3 strain tensor ε has not been established in the literature. To fill this gap, we first derive the symmetry-allowed form of the spin-strain interaction Hamiltonian [see Eq. (3)]. Second, we present numerical results for the six coupling-strength parameters appearing in the spin-strain interaction Hamiltonian (see Table I), which we compute using density functional theory (DFT); we find reasonable agreement with experimental results (see Table II). Third, we propose a setup to measure those two coupling-strength parameters which have not been experimentally characterized yet (Sec. V). Finally, we discuss how the spin-strain interaction can contribute to various applications of NVs in quantum information schemes (Sec. VI). In particular, our results can be applied to design electrical or mechanical schemes to control the magnetically allowed spin transitions of these defects, potentially offering lower power requirements, simplified device layouts, faster spin control, and local addressability of spin qubits.

We formulate our results in terms of the spin-stress interaction as well. We emphasize that our qualitative considerations apply more generally to the whole family of spin-1 electronic states of defects with C_{3v} symmetry. Finally, we note that throughout this work, we describe the interaction between the spin and the mechanical deformation in the framework of linear elasticity theory.

II. PRELIMINARIES

We choose the *cubic reference frame* such that its origin coincides with the vacancy, and the nitrogen is at $(a/4, a/4, a/4)$, with a being the width of the cubic cell. The coordinates

*Corresponding author: palyi@mail.bme.hu

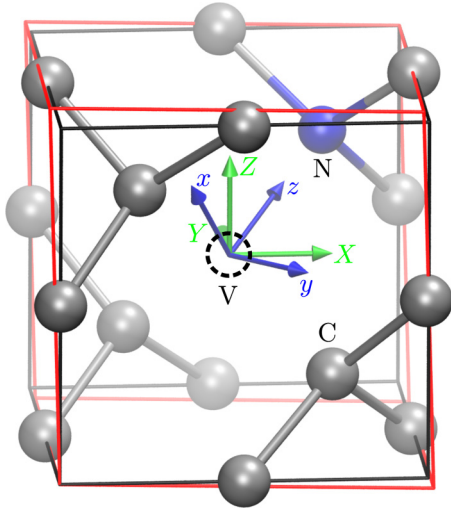


FIG. 1. Nitrogen-vacancy (NV) center in the diamond lattice (Bravais cell depicted as a cube in black). $\{X, Y, Z\}$ defines the cubic reference frame and $\{x, y, z\}$ defines the NV reference frame. Deformation of the diamond crystal is visualized in red for $\epsilon_{xx} = 0.1$ strain component. We use this high strain only for sake of clarity.

in the cubic frame are referred to as X, Y, Z (see Fig. 1). The *NV reference frame* is defined via its three orthonormal basis vectors $\mathbf{e}_z = (1, 1, 1)/\sqrt{3}$, $\mathbf{e}_y = (1, -1, 0)/\sqrt{2}$, and $\mathbf{e}_x = \mathbf{e}_y \times \mathbf{e}_z$. From now on, unless noted otherwise, we use the NV frame, and x, y , and z refer to coordinates in the NV frame. This choice of the reference frame implies that reflection upon the xz plane is a symmetry of the structure. This reflection, together with the threefold rotation around the z axis, generate the point group C_{3v} of the defect.

In the presence of a homogeneous magnetic field $\mathbf{B} = (B_x, B_y, B_z)$, and in the absence of any electric field and strain, the NV spin is described by the following Hamiltonian:

$$H_e/h = DS_z^2 + \gamma_e \mathbf{B} \cdot \mathbf{S}, \quad (1)$$

where h is Planck's constant, $D = 2.87$ GHz is the zero-field splitting, $\gamma_e = 2.8$ MHz/G is the electron gyromagnetic ratio, and $\mathbf{S} = (S_x, S_y, S_z)$ is the vector of spin-1 Pauli matrices. The eigenstates and eigenvalues of S_z will be labeled according to $S_z|m_S e\rangle = m_S|m_S e\rangle$, where $m_S \in \{-1, 0, +1\}$.

The interaction Hamiltonian of a homogeneous electric field $\mathbf{E} = (E_x, E_y, E_z)$ with the NV spin is constrained by the C_{3v} symmetry of the defect, and hence described by [27,38,39]

$$H_E = H_{E0} + H_{E1} + H_{E2}, \quad (2a)$$

TABLE I. Spin-strain (h) and spin-stress (g) coupling-strength parameters calculated from density functional theory. See Appendix B for methodological details. Results are rounded to significant digits.

Parameter	value (MHz/strain)	Parameter	value (MHz/GPa)
h_{43}	2300 ± 200	g_{43}	2.4 ± 0.2
h_{41}	-6420 ± 90	g_{41}	-5.17 ± 0.07
h_{25}	-2600 ± 80	g_{25}	-2.17 ± 0.07
h_{26}	-2830 ± 70	g_{26}	-2.58 ± 0.06
h_{15}	5700 ± 200	g_{15}	3.6 ± 0.1
h_{16}	19660 ± 90	g_{16}	18.98 ± 0.09

TABLE II. Spin-stress coupling-strength parameters: comparison of density functional theory and experimental [34] results. Parameters in the hybrid representation (a_1, a_2 , etc.) are expressed in terms of the parameters in the NV-frame representation (g_{41} , etc.) in the second column. Par. and expt. are abbreviations for “parameters” and “experimental results.”

Par.	Relation	DFT (MHz/GPa)	Expt. [34] (MHz/GPa)
a_1	$\frac{2g_{41}+g_{43}}{3}$	-2.66 ± 0.07	-4.4 ± 0.2
a_2	$\frac{-g_{41}+g_{43}}{3}$	2.51 ± 0.06	3.7 ± 0.2
b	$\frac{-g_{15}+\sqrt{2}g_{16}}{12}$	1.94 ± 0.02	2.3 ± 0.3
c	$\frac{-2g_{15}-\sqrt{2}g_{16}}{12}$	-2.83 ± 0.03	-3.5 ± 0.3
d	$\frac{-g_{25}+\sqrt{2}g_{26}}{12}$	-0.12 ± 0.01	
e	$\frac{-2g_{25}-\sqrt{2}g_{26}}{12}$	0.66 ± 0.01	

$$H_{E0}/h = d_{\parallel} S_z^2 E_z, \quad (2b)$$

$$H_{E1}/h = d'_{\perp} [\{S_x, S_z\}E_x + \{S_y, S_z\}E_y], \quad (2c)$$

$$H_{E2}/h = d_{\perp} [(S_y^2 - S_x^2)E_x + \{S_x, S_y\}E_y]. \quad (2d)$$

Here, the lower indices 0, 1, and 2 refer to the difference in the electron spin quantum numbers (m_S) connected by the corresponding Hamiltonian; e.g., H_{E1} has nonzero matrix elements between $|0e\rangle$ and $|\pm 1e\rangle$. The coefficients $d_{\perp} = 17$ Hz cm/V and $d_{\parallel} = 0.35$ Hz cm/V have been inferred in the experiment of Ref. [38]. However, to our knowledge, the coefficient d'_{\perp} has not been quantified experimentally or theoretically; nevertheless it is expected [27] to have the same order of magnitude as d_{\perp} .

Two remarks on the spin-electric interaction Hamiltonian H_E : (1) The presence of H_{E1} in the spin-electric Hamiltonian is a clear indication that coherent Rabi oscillations within the state pairs $|0e\rangle \leftrightarrow | + 1e\rangle$ and $|0e\rangle \leftrightarrow | - 1e\rangle$ can be driven by an ac electric field. This means, in principle, that any coherent-control experiment where these transitions are driven by ac magnetic field can also be done by replacing the ac magnetic field with an ac electric field, e.g., created by a single metallic gate electrode. To our knowledge, this opportunity which is routinely exploited for various solid-state spin systems [40–43] and is known as *electrically driven spin resonance* or *electric dipole spin resonance*, has been overlooked in the literature in the context of the magnetically allowed $|0e\rangle \leftrightarrow | + 1e\rangle$ and $|0e\rangle \leftrightarrow | - 1e\rangle$ transitions of NVs and similar defects with C_{3v} symmetry. Since electric control might bring significant advantages over magnetic control (simplified device layout, well-confined control fields allowing for local spin addressability, lower power requirements, etc.), this observation provides a strong motivation to characterize the coupling-strength parameter d'_{\perp} of H_{E1} both experimentally and theoretically. (2) The experimental setup we propose in Sec. V to measure spin-stress and spin-strain coupling-strength parameters can be easily adopted to measure d'_{\perp} .

III. SPIN-STRAIN HAMILTONIAN

In our understanding, the spin-strain interaction Hamiltonians used in the literature to characterize the NV (and similar defects with C_{3v} symmetry) are incomplete. A

central result of this work is the most general form of this Hamiltonian that is compatible with the C_{3v} symmetry of the NV. We find that this general symmetry-allowed Hamiltonian is characterized by six independent real *coupling-strength parameters* h_{41} , h_{43} , h_{25} , h_{26} , h_{15} , h_{16} , and has the following form:

$$H_\varepsilon = H_{\varepsilon 0} + H_{\varepsilon 1} + H_{\varepsilon 2}, \quad (3a)$$

$$H_{\varepsilon 0}/h = [h_{41}(\varepsilon_{xx} + \varepsilon_{yy}) + h_{43}\varepsilon_{zz}]S_z^2, \quad (3b)$$

$$H_{\varepsilon 1}/h = \frac{1}{2}[h_{26}\varepsilon_{zx} - \frac{1}{2}h_{25}(\varepsilon_{xx} - \varepsilon_{yy})]\{S_x, S_z\} + \frac{1}{2}(h_{26}\varepsilon_{yz} + h_{25}\varepsilon_{xy})\{S_y, S_z\}, \quad (3c)$$

$$H_{\varepsilon 2}/h = \frac{1}{2}[h_{16}\varepsilon_{zx} - \frac{1}{2}h_{15}(\varepsilon_{xx} - \varepsilon_{yy})](S_y^2 - S_x^2) + \frac{1}{2}(h_{16}\varepsilon_{yz} + h_{15}\varepsilon_{xy})\{S_x, S_y\}, \quad (3d)$$

where $\varepsilon_{ij} = (\partial u_i/\partial x_j + \partial u_j/\partial x_i)/2$ denotes the strain tensor and $\mathbf{u}(\mathbf{r})$ is the displacement field. Similarly to Eq. (2), the subscripts 0, 1, and 2 here refer to the difference in the electron spin quantum numbers m_S connected by the corresponding Hamiltonian. We present an elementary derivation of Eq. (3), as well as a derivation based on group representation theory, in Appendix A.

Note that the symmetry-allowed form of the spin-stress interaction, i.e., when the mechanical deformation is characterized by the 3×3 stress tensor σ instead of strain ε , is completely analogous to Eq. (3). In what follows, we adopt a notation for the spin-stress Hamiltonian H_σ that is analogous to Eq. (3), with the substitutions $\varepsilon \mapsto \sigma$ and $h \mapsto g$:

$$H_\sigma = H_{\sigma 0} + H_{\sigma 1} + H_{\sigma 2}, \quad (4a)$$

$$H_{\sigma 0}/h = [g_{41}(\sigma_{xx} + \sigma_{yy}) + g_{43}\sigma_{zz}]S_z^2, \quad (4b)$$

$$H_{\sigma 1}/h = \frac{1}{2}[g_{26}\sigma_{xz} - \frac{1}{2}g_{25}(\sigma_{xx} - \sigma_{yy})]\{S_x, S_z\} + \frac{1}{2}(g_{26}\sigma_{yz} + g_{25}\sigma_{xy})\{S_y, S_z\}, \quad (4c)$$

$$H_{\sigma 2}/h = \frac{1}{2}[g_{16}\sigma_{xz} - \frac{1}{2}g_{15}(\sigma_{xx} - \sigma_{yy})](S_y^2 - S_x^2) + \frac{1}{2}(g_{16}\sigma_{yz} + g_{15}\sigma_{xy})\{S_x, S_y\}. \quad (4d)$$

Many recent works (e.g., Refs. [19,21,31]) rely on heuristic spin-strain Hamiltonians built on an unjustified analogy between strain and electric field. That approach does not take into account the 3×3 tensor structure of strain, therefore, it provides an incorrect description of the spin-strain interaction, even in the absence shear strain. A recent work [34] uses a spin-stress Hamiltonian based on the 3×3 stress tensor σ ; their Hamiltonian includes four real parameters a_1 , a_2 , b , and c . That Hamiltonian is equivalent to our $H_{\sigma 0} + H_{\sigma 2}$, but incomplete as it lacks the symmetry-allowed term $H_{\sigma 1}$ analogous to Eq. (3c); we provide more details on its relation to our results in Sec. IV. We note that using the incomplete $H_{\sigma 0} + H_{\sigma 2}$ Hamiltonian in Ref. [34] is justified as an approximation since the term $H_{\sigma 1}$ is a small perturbation in the magnetic-field range addressed in those experiments. We also remark that in a very recent work [44], a spin-phonon interaction Hamiltonian incorporating matrix elements between $|0e\rangle$ and $|\pm 1e\rangle$ has been used to describe spin relaxation in NVs.

IV. SPIN-STRAIN PARAMETERS FROM DENSITY FUNCTIONAL THEORY

We use DFT to numerically compute the six coupling-strength coefficients h_{41} , etc., appearing in the spin-strain Hamiltonian (3). The calculations include spin-spin interactions, but exclude spin-orbit effects (for details, see Appendix B.) Methodological details are presented in Appendix B. The results are summarized in Table I. Therein, we also present the spin-stress coupling-strength coefficients g_{41} , etc., which we obtain from the h values using the stiffness tensor of bulk diamond (see Appendix C).

In Table II, we compare the numerical DFT results of Table I to the experimental results of Ref. [34]. In Ref. [34], four out of the six independent spin-stress coupling-strength parameters of the spin-stress interaction Hamiltonian were measured. Reference [34] defines these four spin-stress coupling-strength parameters, denoted as a_1 , a_2 , b , c , in a ‘‘hybrid’’ representation, where the spin-stress Hamiltonian is expressed in terms of the NV-frame components of the spin vector (S_x , S_y , S_z) and the cubic-frame components of the stress tensor (σ_{XX} , σ_{XY} , etc.). To be able to make a comparison between our DFT results and the experimental ones, we now take the notations of Ref. [34], and introduce d , e , \mathcal{N}_x , \mathcal{N}_y , to express our spin-stress Hamiltonian H_σ in Eq. (4) in this hybrid representation:

$$H_{\sigma 0}/h = \mathcal{M}_z S_z^2, \quad (5a)$$

$$H_{\sigma 1}/h = \mathcal{N}_x \{S_x, S_z\} + \mathcal{N}_y \{S_y, S_z\}, \quad (5b)$$

$$H_{\sigma 2}/h = -\mathcal{M}_x (S_x^2 - S_y^2) + \mathcal{M}_y \{S_x, S_y\}, \quad (5c)$$

where

$$\mathcal{M}_z = a_1(\sigma_{XX} + \sigma_{YY} + \sigma_{ZZ}) + 2a_2(\sigma_{YZ} + \sigma_{ZX} + \sigma_{XY}), \quad (6a)$$

$$\mathcal{N}_x = d(2\sigma_{ZZ} - \sigma_{XX} - \sigma_{YY}) + e(2\sigma_{XY} - \sigma_{YZ} - \sigma_{ZX}), \quad (6b)$$

$$\mathcal{N}_y = \sqrt{3}[d(\sigma_{XX} - \sigma_{YY}) + e(\sigma_{YZ} - \sigma_{ZX})], \quad (6c)$$

$$\mathcal{M}_x = b(2\sigma_{ZZ} - \sigma_{XX} - \sigma_{YY}) + c(2\sigma_{XY} - \sigma_{YZ} - \sigma_{ZX}), \quad (6d)$$

$$\mathcal{M}_y = \sqrt{3}[b(\sigma_{XX} - \sigma_{YY}) + c(\sigma_{YZ} - \sigma_{ZX})]. \quad (6e)$$

The relations between the hybrid-representation parameters (a_1 , a_2 , b , c , d , e) and the NV-frame parameters (g_{41} , etc.) are given in the first two columns of Table II. Importantly, $H_{\sigma 0}$ and $H_{\sigma 2}$ are identical to the spin-stress Hamiltonian in Eqs. (1) and (2) of Ref. [34].

In Table II, the DFT results for the cubic-frame spin-strain coupling-strength parameters are listed in the third column, whereas the experimental values [34] are listed in the fourth column.¹ According to Table II, the signs of the DFT and experimental results are the same, and for all four parameters

¹Note that with respect to the values quoted in Ref. [34], the values in the fourth column of Table II have an inverted sign because of the different sign convention for the stress tensor: we assign a negative stress to compression.

determined from the experiment, the order of magnitude matches well with that of the DFT result. This suggests that the DFT method applied here captures the key mechanism of interaction between the electron spin and the mechanical deformation, and gives confidence in the predictions for the previously omitted parameters d and e .

V. POSSIBLE METHODS TO MEASURE THE SPIN-STRESS PARAMETERS

To our knowledge, the spin-stress coupling strength parameters g_{25} and g_{26} have not yet been measured. In this section, we propose a method that allows to determine those in an experiment which combines the controlled application of mechanical stress and ODMR. The method, inspired by the experiment of Ref. [45], requires a finite magnetic field along the NV axis, which tunes the system to the ground-state level anticrossing (GSLAC) where the $| -1e \rangle$ and $| 0e \rangle$ electronic states are approximately degenerate, $B_z \approx B_g \equiv D/\gamma_e \approx 1024$ G. In that setting, mechanical stress can induce strong mixing of the spin eigenstates of the coupled electron-nuclear system via the coupling-strength parameters g_{25} and g_{26} . In turn, the spin dynamics governed by this mixing can be detected in a time-resolved fashion, via photoluminescence-based optical readout of the NV spin system. First, in Sec. VA, we introduce our model, and show that the mechanical stress can be thought of as an extra contribution to the external magnetic field [see Eq. (12)]. Second, in Sec. VB, we describe an arrangement that can be used to determine the axial spin-stress coupling-strength parameters g_{41} and g_{43} . Third, in Sec. VC, we outline the experiment to determine the transverse coupling-strength parameters g_{25} and g_{26} .

A. Effective magnetic field due to mechanical stress

The measurement schemes described here work in the vicinity of the GSLAC, where the $| -1e \rangle$ and $| 0e \rangle$ electronic spin levels are nearly degenerate. This is where the stress-induced terms of $H_{\sigma 1}$, which are typically much smaller than the zero-field spin splitting D , are most effective in mixing these two electronic spin states. Due to the presence of the N nuclear spin and hyperfine interaction, there is a hyperfine structure of the energy spectrum at the GSLAC [46]. This is illustrated for the case of an ^{14}N nuclear spin in Fig. 2: instead of two electron spin levels crossing at $B_z = B_g$, there are six levels, with two level pairs showing hyperfine-induced anticrossings. We focus on the case when the N atom of the NV center is an ^{14}N ; the analysis can be generalized straightforwardly for the ^{15}N case [45,47].

We assume that a magnetic field $B_z \approx B_g$ is applied, aligned with the NV axis. Formally we write the magnetic field vector as $\mathbf{B} = (B_x, B_y, B_z)$, but we will consider only the case $B_x = B_y = 0$. The nine-dimensional Hamiltonian describing the coupled electron-nuclear system in the presence of the magnetic field and mechanical stress reads as

$$H = H_e + H_\sigma + H_n + H_{hf}, \quad (7)$$

where H_e is defined in Eq. (1), H_σ is defined in Eq. (4), H_n describes the nuclear Zeeman effect and the quadrupole

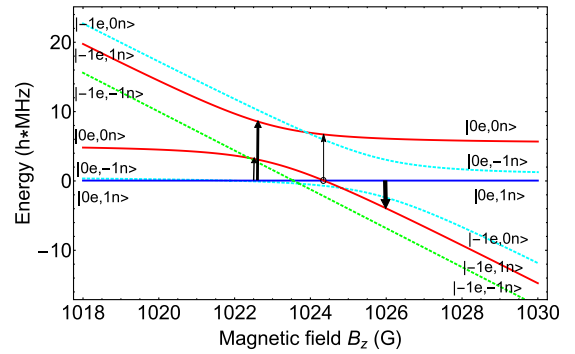


FIG. 2. Level structure of the ^{14}NV at the GSLAC as a function of the axial magnetic field B_z . All transverse magnetic field components and stress are zero, $B_x = B_y = 0$, $\sigma = 0$. The circle marks the crossing that serves to identify the stress coupling coefficients g_{25} , g_{26} . The levels coupled by the hyperfine interaction are shown with the same color (red solid; light blue dashed). The arrows indicate the bright radio-frequency magnetic transitions at the corresponding values of the magnetic field. In the absence of mechanical stress, the dashed lines are invisible in optically detected magnetic resonance.

moment of the $I = 1$ spin of the ^{14}N via

$$H_n/h = -\gamma_n B_z I_z + Q I_z^2, \quad (8)$$

and H_{hf} describes the hyperfine interaction via

$$H_{hf}/h = A_{\parallel} S_z I_z + A_{\perp} (S_x I_x + S_y I_y). \quad (9)$$

We use the eigenstates of I_z as the basis for the nuclear spin states, labeled according to $I_z |m_I n\rangle = m_I |m_I n\rangle$, where $m_I \in \{-1, 0, +1\}$. Note that in H_n we use $\mathbf{B} = (0, 0, B_g)$ for simplicity. The literature values of the coefficients [48–51] are $Q = -4.95$ MHz, $A_{\parallel} = -2.14$ MHz, $A_{\perp} = -2.7$ MHz.

The six low-energy eigenstates of the 9×9 Hamiltonian H are shown in Fig. 2 as a function of the axial magnetic field B_z , in the vicinity of the GSLAC. For this plot, zero stress is assumed. Solid lines highlight the three levels that will be utilized to determine the spin-stress coupling-strength parameters. In Fig. 2, anticrossings are induced by hyperfine interaction, but far from the anticrossings the depicted energy eigenstates are eigenstates of S_z and I_z to a good approximation, and therefore are labeled accordingly, as $|m_{Se}, m_{In}\rangle$.

When describing the effect of a nonzero mechanical stress, it is possible and helpful to introduce the notion of an *effective magnetic field* vector (Φ_x, Φ_y, Φ_z) , which describes the combined effect of the actual magnetic field and the stress-induced terms in the Hamiltonian. To see this, let us first focus on the electronic degree of freedom and the two-dimensional low-energy electron spin subspace at the GSLAC. The electronic Hamiltonian in this two-dimensional subspace is expressed using the corresponding projector $P = |0e\rangle\langle 0e| + |-1e\rangle\langle -1e|$ as

$$P H_e P = h\gamma_e \begin{pmatrix} 0 & \frac{B_x - iB_y}{\sqrt{2}} \\ \frac{B_x + iB_y}{\sqrt{2}} & B_g - B_z \end{pmatrix}. \quad (10)$$

In the presence of a nonzero stress, described by the matrix σ , this Hamiltonian generalizes to

$$P(H_e + H_\sigma)P = h\gamma_e \begin{pmatrix} 0 & \frac{\Phi_x - i\Phi_y}{\sqrt{2}} \\ \frac{\Phi_x + i\Phi_y}{\sqrt{2}} & B_g - \Phi_z \end{pmatrix}, \quad (11)$$

where we introduced the effective magnetic field components

$$\Phi_x = B_x + \frac{g_{25}}{4\gamma_e}(\sigma_{xx} - \sigma_{yy}) - \frac{g_{26}}{2\gamma_e}\sigma_{xz}, \quad (12a)$$

$$\Phi_y = B_y - \frac{g_{25}}{2\gamma_e}\sigma_{xy} - \frac{g_{26}}{2\gamma_e}\sigma_{yz}, \quad (12b)$$

$$\Phi_z = B_z - \frac{g_{41}}{\gamma_e}(\sigma_{xx} + \sigma_{yy}) - \frac{g_{43}}{\gamma_e}\sigma_{zz}. \quad (12c)$$

These expressions reveal that the mechanical stress can be thought of as an extra contribution to the applied magnetic field.

B. Measuring the axial spin-stress parameters g_{41} , g_{43}

Our proposed experiment to determine g_{41} and g_{43} combines a controlled application of static uniaxial stress, and ODMR [45], in an axial magnetic field that tunes the NV spin system to the GSLAC. Note that these coupling-strength parameters have already been experimentally characterized by a different method in Ref. [34].

The first stage of our proposed experiment is the observation of certain parts of the hyperfine level structure shown in Fig. 2. At this stage, no mechanical stress is applied, and a conventional ODMR spectroscopy experiment [45] is carried out, as explained below. In the vicinity of the GSLAC, at $(B_x, B_y, B_z) \approx (0, 0, B_g)$, the coupled electron-nuclear spin system is initialized to the state $|\psi(0)\rangle = |0e, -1n\rangle$ (blue solid line in Fig. 2) with an optical pulse. Then, an ac magnetic pulse of a given frequency f , amplitude B_{ac} , and duration τ is applied. On the one hand, if that magnetic pulse is off resonant with respect to all energy eigenstates in Fig. 2, then the spin system remains in its initial state $|\psi(\tau)\rangle \propto |0e, -1n\rangle$. Then, a readout optical pulse at time $t = \tau$ will result in significant photoluminescence which is measured. Note that the photoluminescence after the readout pulse is proportional to the occupation probability of the $|0e\rangle$ electron spin state, i.e., to the quantity $\sum_{m_I} |(0e, m_I n | \psi(\tau))|^2$. On the other hand, if the magnetic field pulse is resonant with one of the transitions in Fig. 2, then it can change the initial state to a state $|\psi(\tau)\rangle$ that contains a reduced weight of the $|0e\rangle$ state, and thereby the photoluminescence signal decreases.

To quantify this drop in the photoluminescence signal upon resonant excitation, we will use the quantity

$$C = 1 - \sum_{m_I=-1,0,1} |(0e, m_I n | \psi(\tau))|^2, \quad (13)$$

and call it the *photoluminescence contrast*. This quantity characterizes how effective the magnetic pulse is in inducing spin transitions: the value of C is zero for an off-resonant magnetic pulse, and can take values between 0 and 1 for a resonant magnetic pulse.

The black curves in Fig. 3(b) visualize the predicted outcome of this experiment using the photoluminescence contrast C (cf. Fig. 2 of Ref. [45]). Our Fig. 3(b) demonstrates that key

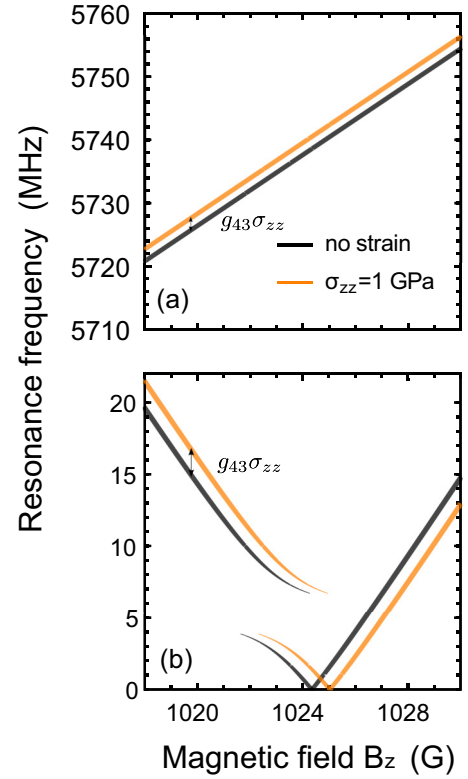


FIG. 3. Effect of mechanical stress on the photoluminescence contrast in optically detected magnetic resonance of an ^{14}NV center. Black: no stress, orange: $\sigma_{zz} = 1$ GPa. The curves show the dependence of hyperfine transition frequencies as function of the axial magnetic field B_z in the vicinity of the GSLAC. The thickness of each curve is proportional to the photoluminescence contrast C [Eq. (13)]; maximal thickness corresponds to $C = 1$. (a) High-energy transitions to $|1e\rangle$ spin states. (b) Low-energy transitions within the subspace of $|0e\rangle$ and $|-1e\rangle$.

features of the hyperfine structure of the spin levels of Fig. 2 can be mapped using this experimental technique. To generate this plot, we calculated the five resonant transition frequencies from the spectral gaps in Fig. 2. We plot these five curves in Fig. 3(b), where the thickness of each curve is rescaled by the corresponding photoluminescence contrast C . Hence, the black curves in Fig. 3(b) reveal that for a given magnetic field, at most two out of the five transitions are bright. The bright transitions at three specific B_z values are also indicated in Fig. 2. We calculated the photoluminescence contrast C based on standard two-level Rabi dynamics in the rotating wave approximation, assuming resonant driving frequency f , a magnetic pulse strength $b = g\mu_B B_{ac}\tau/h = \sqrt{2}/4$, and the ac magnetic field vector being aligned with the x axis. Note that the above pulse strength b corresponds to an exact electron-spin π pulse away from the GSLAC.

The second stage of the experiment is to repeat this ODMR spectroscopy in the presence of uniaxial z -directional strain, $\sigma_{zz} \neq 0$. The predicted photoluminescence contrast for the case of $\sigma_{zz} = 1$ GPa is shown by the orange curves in Fig. 3(b). Apparently, the spectrum shifts along the B_z axis. Measuring this shift reveals the spin-stress coupling-strength parameter g_{43} . In fact, simple analytical expressions can be obtained for

the locations of the ODMR resonances, including the effect of the considered uniaxial strain. By projecting the 9×9 Hamiltonian H to the two-dimensional subspace of $|0e, 0n\rangle$ and $|-1e, 1n\rangle$, and diagonalizing the resulting 2×2 Hamiltonian, we obtain the resonance frequencies corresponding to the bright low-frequency transitions (blue \rightarrow red transitions in Fig. 2):

$$f_{\pm} = \left| \frac{1}{2} \left[-A_{\parallel} + D \left(1 + \frac{\gamma_n}{\gamma_e} \right) - Q - \gamma_e \Phi_z \right] \pm \sqrt{A_{\perp}^2 + \frac{1}{4} \left[A_{\parallel} - D \left(1 - \frac{\gamma_n}{\gamma_e} \right) - Q + \gamma_e \Phi_z \right]^2} \right|. \quad (14)$$

For magnetic fields significantly below the GSLAC, e.g., around $B_z = 1019$ G in Fig. 3(b), the bright transition resonance frequency can be approximated by making a zeroth-order expansion of f_{+} [see Eq. (14)] in A_{\perp} , and substituting Eq. (12c) to the result, yielding

$$f_{+} \approx -A_{\parallel} + D - \gamma_e B_z + g_{43} \sigma_{zz}. \quad (15)$$

This implies that g_{43} can be directly calculated from the measured stress-induced shift of the resonance frequency at a given magnetic field (e.g., $B_z = 1019$ G) via

$$g_{43} = \frac{f_{+}(B_z, \sigma_{zz}) - f_{+}(B_z, 0)}{\sigma_{zz}}. \quad (16)$$

The third and last stage of the experiment is to obtain g_{41} by repeating this ODMR spectroscopy in the presence of uniaxial stress along $\mathbf{n} = (1, 1, 0)/\sqrt{2}$. In that case, the stress tensor reads as $\sigma_{ij} = n_i n_j \sigma$, hence, the three components $\sigma_{xx} = \sigma_{yy} = \sigma_{xy} = \sigma/2$ are nonzero. Because of the nonzero off-diagonal component σ_{xy} , a nonzero effective magnetic field component Φ_y is present [see Eq. (12b)], seemingly complicating the previous analysis. However, assuming that our DFT predictions in Table I for the coupling-strength orders of magnitude are correct, the effect of this σ_{xy} -induced effective transverse magnetic field component on the energy spectrum can be neglected away from the anticrossing, e.g., at $B_z = 1019$ G. Therefore, in this situation the stress-induced shift of the resonance frequency can be translated to the coupling-strength parameter g_{41} via

$$g_{41} = \frac{f_{+}(B_z, \sigma) - f_{+}(B_z, 0)}{\sigma}. \quad (17)$$

We note that these coupling-strength coefficients g_{41} and g_{43} can also be determined by utilizing the high-energy $|1e, 1n\rangle$ spin state at the GSLAC and the corresponding ~ 6 GHz ac magnetic field pulses. This is illustrated by Fig. 3(a), where the photoluminescence contrast corresponding to the $|0e, 1n\rangle \rightarrow |1e, 1n\rangle$ transition is shown in the absence (black) and presence (orange) of z -directional mechanical stress. The relation between the coupling-strength parameters and the shift of the resonance frequency is the same as for the low-energy transitions [see Eqs. (16) and (17)].

C. Measuring the transverse spin-stress parameters g_{25} , g_{26}

Here, we propose and quantitatively analyze a method for measuring the transverse spin-stress coupling-strength coefficients g_{25} , g_{26} . Similarly to the method in the preceding sub-

section, this method also works in the vicinity of the GSLAC. It is based on the experiment discussed and implemented in Sec. IV of Ref. [45], where Larmor-precession spin dynamics was used to precisely measure the magnetic-field component perpendicular to the NV axis (see, e.g., their Fig. 3). Here, we focus on how to measure the coupling strengths g_{25} , g_{26} in the case when the magnetic field is aligned with the NV axis. Our method relies on the observation of Larmor-precession spin dynamics, which is affected by stress via the spin-stress interaction described by Eq. (4). The role of the transverse magnetic field components B_x and B_y in the experiment of Ref. [45] is played by the stress-induced transverse effective magnetic field components Φ_x and Φ_y in our setup.

First, recall the experimental scheme of Ref. [45] for the special case when B_z is tuned to the blue-red level crossing in Fig. 2, $B_z = B_c$, denoted by a circle. The two states that meet at the crossing are, to a good approximation, $|0e, 1n\rangle$ and $|\chi\rangle = \frac{1}{\sqrt{1+\alpha^2}}(\alpha|0e, 0n\rangle + |-1e, 1n\rangle)$, where $\alpha = \frac{\gamma_e A_{\perp}}{Q\gamma_e - D\gamma_n} \approx 0.5$. For the readout, it will prove important that the weight of $|\chi\rangle$ in the $|0e\rangle$ subspace is $|\langle 0e, 0n|\chi\rangle|^2 \approx 0.2$, significantly lower than 1. In the presence of a small transverse magnetic field, the blue-red level crossing in Fig. 2 is split to an anticrossing, due to a coupling Hamiltonian matrix element between these states, which enters the two-level Hamiltonian of $|0e, 1n\rangle$ and $|\chi\rangle$ as

$$H_L = \frac{h\gamma_e}{\sqrt{2(1+\alpha^2)}} \begin{pmatrix} 0 & B_x - iB_y \\ B_x + iB_y & 0 \end{pmatrix}. \quad (18)$$

In this setup, the experiment starts with an optical pulse that initializes the spin system in $|\psi(0)\rangle = |0e, 1n\rangle$ at $t = 0$. Because of the finite transverse magnetic field in Eq. (18), this initial state is not an energy eigenstate, and therefore the time evolution $|\psi(t)\rangle$ exhibits complete Larmor-precession cycles between the two states $|0e, 1n\rangle$ and $|\chi\rangle$. To observe this Larmor precession, the photoluminescence contrast $C(\tau)$ was measured [45] as a function of the waiting time τ following the initialization. This photoluminescence contrast $C(\tau)$ reveals the Larmor precession since the state $|\chi\rangle$ is mostly outside the $|0e\rangle$ subspace. The frequency of this Larmor precession is derived from Eq. (18):

$$f_L = \sqrt{\frac{2}{1+\alpha^2}} \gamma_e \sqrt{B_x^2 + B_y^2}. \quad (19)$$

Here, we suggest to adopt this scheme to characterize the effective transverse magnetic field components Φ_x and Φ_y defined in Eq. (12), and thereby measure the spin-stress coupling-strength coefficients g_{25} and g_{26} . For simplicity, we make the following specifications. First, we take $B_x = B_y = 0$. Second, for an arbitrary uniaxial stress $\sigma_{ij} = \sigma n_i n_j$, defined by its direction $\mathbf{n} = (n_x, n_y, n_z)$ and magnitude σ , we suggest to tune B_z to the ‘‘virtual crossing point,’’ i.e., to a value $B_z = \tilde{B}_c$, where the energy eigenvalues of $|0e, 1n\rangle$ and $|\chi\rangle$ would be degenerate in the virtual situation when the transverse effective magnetic field components are turned off, $\Phi_x = \Phi_y = 0$. That is guaranteed for $\Phi_z = B_c$, which, together with Eq. (12c), implies

$$\tilde{B}_c = B_c + \frac{g_{41}(n_x^2 + n_y^2) + g_{43}n_z^2}{\gamma_e} \sigma. \quad (20)$$

This simple expression reveals that this virtual crossing point can be identified once the parameters g_{41} and g_{43} have been measured, e.g., using the method of the preceding section.

At this virtual crossing point, the role of the transverse effective magnetic fields Φ_x and Φ_y is completely analogous to the role of B_x and B_y in Ref. [45]. Namely, they force the spin system initialized in $|0e, 1n\rangle$ to exhibit complete Larmor precessions between the states $|0e, 1n\rangle$ and $|\chi\rangle$, with the Larmor frequency [cf. Eq. (19)]

$$f_L = \sqrt{\frac{2}{1 + \alpha^2}} \gamma_e \sqrt{\Phi_x^2 + \Phi_y^2}. \quad (21)$$

From this, and using Eq. (12) for the effective magnetic fields, we find

$$f_L = \sqrt{\frac{\frac{g_{25}^2}{4} n_{\perp}^4 + g_{26}^2 n_z^2 n_{\perp}^2 + g_{25} g_{26} n_x n_z (3n_y^2 - n_x^2)}{2(1 + \alpha^2)}} |\sigma|, \quad (22)$$

with $n_{\perp} = \sqrt{n_x^2 + n_y^2}$.

Our result (22) allows the identification of the coefficients g_{25} and g_{26} by applying the uniaxial stress in different directions and then measuring the Larmor precession frequency. For example, the absolute value of g_{25} can independently be measured by applying the uniaxial stress in the direction $\mathbf{n} = (1, 1, 0)/\sqrt{2}$. In that case, Eq. (22) implies that this coupling-strength parameter is deduced from the measured Larmor frequency via

$$|g_{25}| = \sqrt{8(1 + \alpha^2)} \frac{f_L}{|\sigma|} \approx 3.17 \frac{f_L}{|\sigma|}. \quad (23)$$

Analogously, the absolute value of g_{26} can independently be measured with the uniaxial stress applied in the direction $\mathbf{n} = (\sqrt{3}, 1, 1)/\sqrt{5}$; for that case, we find

$$|g_{26}| = \frac{\sqrt{10(1 + \alpha^2)}}{2} \frac{f_L}{|\sigma|} \approx 1.77 \frac{f_L}{|\sigma|}. \quad (24)$$

We note that this procedure only allows us to determine the absolute values of the coupling-strength coefficients. Nevertheless, it is straightforward to generalize the above procedure to determine the signs of the coefficients by utilizing a finite transverse magnetic field. For example, following up on our first example above, let us assume that we apply compressive uniaxial strain $\sigma < 0$ along $\mathbf{n} = (1, 1, 0)/\sqrt{2}$. If the sign of g_{25} is indeed negative, as indicated by our DFT results in Table I, then the transverse effective magnetic field components read as $\Phi_x = 0$ and $\Phi_y = B_y - p|\sigma|$, with $p > 0$. Hence, according to Eq. (22), the Larmor precession is slowed down gradually as a magnetic field component along the y axis is switched on. On the other hand, if the sign of g_{25} is positive, then a small y -directional magnetic field will speed up the Larmor precession.

An important assumption behind our measurement scheme is that the Larmor precessions at frequency f_L are observable. Note that if the applied stress is too low, then the Larmor precession is too slow compared to its damping timescale governed by the interaction with the neighboring C-13 nuclear spins [45], and thereby the Larmor frequency cannot be deduced from the experiment. Combining this consideration with the experimental data of Ref. [45], we can estimate that

a stress of at least ~ 0.5 GPa should be applied to make this measurement scheme feasible. The estimation goes as follows. In Fig. 3(d) of Ref. [45], Larmor precessions with $f_L \lesssim 0.4$ MHz are resolved. From Eqs. (23) and (24), and the results for g_{25} and g_{26} tabulated in Table I, we estimate that the minimal stress required for observable Larmor precession is 0.58 GPa for the g_{25} measurement, and 0.27 GPa for the g_{26} measurement.

VI. DISCUSSION

A. Potential applications

Time-dependent mechanical deformation for resonant spin control. Coherent spin control in NVs via ac mechanical deformation has been demonstrated with ~ 1 MHz Rabi frequency for the magnetically forbidden $|-1e\rangle \leftrightarrow |1e\rangle$ transition [20]. Our results imply that the other two, magnetically allowed, transitions, $|0e\rangle \leftrightarrow |\pm 1e\rangle$, can also be induced in a similar fashion. This suggests that, in principle, the ac magnetic field used routinely for spin control in NV-based experiments can be substituted by ac mechanical driving. From the spin-strain Hamiltonian H_e of Eq. (3), we estimate that an ac strain ε_{xx} with an amplitude of 0.01 can provide mechanically induced Rabi oscillations for the magnetically allowed transitions with a Rabi frequency of ~ 5 MHz.

Time-dependent electric fields for resonant spin control. According to Eq. (2), an externally induced electric field interacts with the NV spin, allowing for coherent electric control of all three spin transitions of the NV. Electric control of the magnetically forbidden transition has been demonstrated in SiC [43], but that of the magnetically allowed transitions has yet to be achieved. In Ref. [43], electrical Rabi frequencies of ~ 1 MHz were realized for the magnetically forbidden transition. This Rabi frequency is proportional to the coupling-strength parameter d_{\perp} . Furthermore, from the dielectric strength of SiC it was estimated that ~ 60 MHz electrical Rabi frequencies should be reachable, comparable to magnetic spin control with millitesla driving strength [52,53]. Noting that the d_{\perp} parameter and the dielectric strength are similar for NV centers in diamond, and the d'_{\perp} parameter is expected [27] to be of the same order of magnitude as d_{\perp} , we speculate that the electrical Rabi frequencies for the magnetically allowed transitions in diamond NV centers could also reach a few tens of MHz.

Electrically driven, mechanically assisted spin resonance using piezoelectric elements. Our results regarding the spin-strain coupling in C_{3v} symmetric defects promote a new way of using electric signals for coherent control, for all three transitions between the spin-1 basis states. Dynamical mechanical deformation can be created by ac electric fields (voltages) via piezoelectric elements attached to the diamond crystal, e.g., a ZnO layer. The functionality of such arrangements has already been experimentally demonstrated using interdigital transducers serving as transmitters and receivers of surface acoustic waves of the diamond crystal [35,36]. The magnitude of strain created by the ac electric field could further be enhanced using mechanical cavity resonators [54] for the surface acoustic waves. The mechanical waves, when tuned to resonance with the defect spin transition frequency, can then drive coherent spin Rabi oscillations. This working principle

allows for devices where coherent control of the defect spins is performed via electrically driven, mechanically assisted spin resonance.

B. Open problems

Experimental characterization of the spin-strain and the spin-electric parameters. As discussed above, the spin-strain (spin-stress) coupling-strength parameters of $H_{\varepsilon 1}$ ($H_{\sigma 1}$), namely h_{25} and h_{26} (g_{25} and g_{26} , or d and e , depending on the representation), are yet to be characterized experimentally. Similarly, the corresponding spin-electric coupling-strength coefficient [27] d'_1 in Eq. (2) is yet to be measured. We emphasize the technological relevance of these parameters: the terms they multiply in the Hamiltonian can induce magnetically allowed spin transitions, i.e., of the $|0e\rangle \leftrightarrow |\pm 1e\rangle$ type; therefore, for systems where these parameters are sufficiently strong, ac electric or ac mechanical driving could substitute the ac magnetic field that is routinely used in most coherent spin-control experiments.

Quantitative description of mechanically and electrically driven electron spin resonance. The static spin-strain Hamiltonian (3) and the DFT-based coupling-strength parameters in Table I can be used to estimate the timescale (Rabi time) of spin control for an ac mechanical drive with a given strain pattern. However, it is known from the theory of spin-orbit-mediated electrically driven spin resonance [42,55] that even if an electric field does not modify the spin Zeeman splitting, it can induce transition between spin states. Hence, it is expected that an accurate description of mechanically or electrically driven spin resonance for the NV, which probably involves electronic spin-spin and spin-orbit interactions, requires a careful treatment of dynamical effects.

Interaction of strain and electric fields with nuclear spins. The coherence time of the nuclear spin of the N atom in the NV exceeds that of the ground-state electronic spin, and can be used as a long-lived quantum memory [56]. Furthermore, the NV can interact with ^{13}C nuclear spins located in its vicinity. These highly coherent nuclear spins are heavily exploited in NV-based quantum-control experiments [22–24,45,57,58], which is a strong motivation to understand the interaction of solid-state nuclear spins with electric and strain fields. Important steps in this direction have already been taken [59–64], but the experimental and theoretical characterization of the spin-electric and spin-strain interactions for NV nuclear spins is yet to be done.

We anticipate that the nature of the problem is qualitatively different for (i) a spin- $\frac{1}{2}$ nuclear spin, e.g., of a ^{15}N or a ^{13}C atom, and (ii) a nuclear spin that is larger than $\frac{1}{2}$, e.g., of a ^{14}N atom. In case (i) the nuclear spin does not interact directly with electric or strain fields [65]. However, these fields do interact with the electronic spin, which can serve as a quantum transducer that translates these fields to the nucleus via the hyperfine interaction [50,57,60,61,63,66] (Knight field). In case (ii), the nuclear spin has a nonzero electric quadrupole moment, and therefore can interact directly with electric and strain fields via the local electric-field gradient [61,65]. Then, the direct interaction and the hyperfine-mediated interaction will compete. In both cases (i) and (ii), the results of this work

can serve as a starting point to evaluate the hyperfine-mediated contribution.

VII. CONCLUSIONS

We have established the spin-strain and spin-stress interaction Hamiltonians for the NV ground state, and numerically determined the six independent parameters of this Hamiltonian using density functional theory. Focusing on the new Hamiltonian term $H_{\varepsilon 1}$ identified in this work, we proposed an NV-based experimental setup where spin effects caused by a static mechanical deformation can be observed, and suggested coherent mechanical or electric spin control of the magnetically allowed spin transitions. All qualitative considerations of this work should hold for the whole family of defects with C_{3v} symmetry and spin-1 electronic states.

ACKNOWLEDGMENTS

We thank A. Auer, M. Barson, M. Doherty, A. Falk, J. Heremans, V. Ivády, J. Michl, S. Sangtawesin, D. Szaller, G. Thiering, and B. Zhou for helpful discussions. A.P. is supported by the National Research Development and Innovation Office of Hungary (NKFIH) Grants No. 105149 and No. 124723, and the ÚNKP-17-4-III New National Excellence Program of the Ministry of Human Capacities of Hungary. A.G. thanks for the support of the EU Commission in the DIADEMS project (Grant No. 611143). This work was supported by NKFIH within the Quantum Technology National Excellence Program (Project No. 2017-1.2.1-NKP-2017- 00001). V.O.S. and G.B. are supported by the DFG within the collaborative research center SFB 767.

APPENDIX A: SYMMETRY ANALYSIS OF THE SPIN-STRAIN HAMILTONIAN

In this Appendix, we describe two derivations of the symmetry-allowed spin-strain Hamiltonian H_{ε} of Eq. (3). The first derivation is an elementary one, without reference to group representation theory, whereas the second one builds upon concepts of the latter. The two methods yield the same result Eq. (3).

1. Elementary derivation

Our goal is to find the most general form of the Hamiltonian describing the interaction between a homogeneous strain and the ground-state spin (spin-1) of the NV. More precisely, we aim at finding the most general form of the interaction that is (i) allowed by the requirement of time-reversal symmetry, (ii) allowed by the spatial symmetries (C_{3v}) of the structure, (iii) linear in the elements of the strain tensor ε .

The interaction Hamiltonian should be quadratic in the components of the spin vector $S = (S_x, S_y, S_z)$, as time-reversal symmetry changes the sign of those, and the interaction Hamiltonian should be invariant upon time reversal. Our S is dimensionless, fulfilling $S^2 = 2$.

Therefore, our starting point is the Hamiltonian

$$H_{\varepsilon} = \sum_{\alpha, \beta, \gamma, \delta \in \{x, y, z\}} h_{\alpha\beta\gamma\delta} S_{\alpha} S_{\beta} \varepsilon_{\gamma\delta}, \quad (\text{A1})$$

where h is a four-dimensional matrix with real entries. Apparently, h has 81 independent elements; this will now be reduced, first without invoking any symmetries of the considered system.

To this end, we exploit the fact the nine-element set $\{S_\alpha S_\beta | \alpha, \beta \in \{x, y, z\}\}$ is overcomplete (linearly dependent) in the six-dimensional vector space of 3×3 Hermitian time-reversal-invariant matrices. A six-element basis of that vector space is provided by, e.g., $(1, \frac{1}{2}\{S_x, S_y\}, \frac{1}{2}\{S_y, S_z\}, \frac{1}{2}\{S_z, S_x\}, S_z^2, S_x^2 - S_y^2) \equiv (\Sigma_0, \Sigma_1, \dots, \Sigma_5)$. We will neglect the unit matrix Σ_0 from now. Furthermore, we will refer to Σ as a map $(S_x, S_y, S_z) \mapsto \Sigma(S) := (\Sigma_1, \Sigma_2, \dots, \Sigma_5)$.

A further simplification is allowed by the fact that the strain tensor is symmetric. Therefore it can be thought of as a six-dimensional column vector $\epsilon = (\epsilon_{xx}, \epsilon_{yy}, \epsilon_{zz}, \epsilon_{yz}, \epsilon_{zx}, \epsilon_{xy})^T$. We will consider ϵ as a function that maps the strain tensor to a six-dimensional vector $\epsilon \mapsto \epsilon(\epsilon)$.

Using these simplifications, we can express the most general Hamiltonian as

$$H_\epsilon = \sum_{n=1}^5 \sum_{v=1}^6 h_{nv} \Sigma_n \epsilon_v, \quad (\text{A2})$$

where h is a 5×6 matrix with real entries, i.e., it is characterized by only 30 independent elements.

We will now further reduce this number using the spatial symmetry of the NV. Its symmetries are the isometries in the group C_{3v} . Those are generated by a threefold rotation around the z axis, \mathcal{R} , and the reflection on the xz plane, \mathcal{M} . These isometries are represented on a position vector by the 3×3 matrices

$$R = \begin{pmatrix} \cos \frac{2\pi}{3} & -\sin \frac{2\pi}{3} & 0 \\ \sin \frac{2\pi}{3} & \cos \frac{2\pi}{3} & 0 \\ 0 & 0 & 1 \end{pmatrix} \quad (\text{A3})$$

and

$$M = \begin{pmatrix} 1 & 0 & 0 \\ 0 & -1 & 0 \\ 0 & 0 & 1 \end{pmatrix}, \quad (\text{A4})$$

respectively.

A point isometry transforming the structure also transforms the associated physical quantities. For us, one of the relevant quantities is the strain tensor, which is transformed as $\epsilon \mapsto R\epsilon R^{-1}$ and $\epsilon \mapsto M\epsilon M^{-1}$. The other relevant quantity is the spin vector, which transforms as a pseudovector (or axial vector). That is, the rotation is represented on the spin as $S \mapsto RS$, but the reflection is represented as $S \mapsto M'S$ with

$$M' = \begin{pmatrix} -1 & 0 & 0 \\ 0 & 1 & 0 \\ 0 & 0 & -1 \end{pmatrix}. \quad (\text{A5})$$

We require that the Hamiltonian is invariant against the transformations of the point group of the structure; formally, that is written as

$$\sum_{n=1}^5 \sum_{v=1}^6 h_{nv} \Sigma_n(S) \epsilon_v(\epsilon) = \sum_{n=1}^5 \sum_{v=1}^6 h_{nv} \Sigma_n(RS) \epsilon_v(R\epsilon R^{-1}) \quad (\text{A6})$$

and

$$\sum_{n=1}^5 \sum_{v=1}^6 h_{nv} \Sigma_n(S) \epsilon_v(\epsilon) = \sum_{n=1}^5 \sum_{v=1}^6 h_{nv} \Sigma_n(M'S) \epsilon_v(M\epsilon M^{-1}). \quad (\text{A7})$$

Both of these equations form a homogeneous linear set of 30 equations, with the 30 h_{nv} coupling-strength coefficients being the unknowns. Hence, these equations establish linear relationships between the various h_{nv} coefficients, that is, they reduce the number of free parameters in the Hamiltonian.

These equations can be solved, e.g., symbolically using computer algebra. Inserting the solutions to H_ϵ yields our symmetry-allowed spin-strain interaction Hamiltonian of Eq. (3).

2. Derivation based on group representation theory

The C_{3v} symmetry group of the NV has three irreducible representations (irreps): the trivial 1D irrep A_1 , the 1D irrep A_2 , and the 2D irrep E . The quadratic spin-component combinations that transform according to the trivial A_1 irrep are

$$f_{A_1,1}^{(\text{spin})} = S_x^2 + S_y^2, \quad (\text{A8})$$

$$f_{A_1,2}^{(\text{spin})} = S_z^2. \quad (\text{A9})$$

Analogously, the linear strain-component combinations transforming as A_1 are

$$f_{A_1,1}^{(\text{strain})} = \epsilon_{xx} + \epsilon_{yy}, \quad (\text{A10})$$

$$f_{A_1,2}^{(\text{strain})} = \epsilon_{zz}. \quad (\text{A11})$$

We will refer to the number of these combinations as $n(A_1) = 2$. There are no such combinations transforming according to A_2 , i.e., $n(A_2) = 0$. The quadratic spin-component combinations forming 2D vectors, which transform according to the 2D irrep E , are

$$f_{E,1}^{(\text{spin})} = \begin{pmatrix} S_x^2 - S_y^2 \\ -\{S_x, S_y\} \end{pmatrix}, \quad (\text{A12})$$

$$f_{E,2}^{(\text{spin})} = \begin{pmatrix} \{S_x, S_z\} \\ \{S_y, S_z\} \end{pmatrix}. \quad (\text{A13})$$

Analogously, the linear strain-component combinations forming 2D vectors, which transform according to E , are

$$f_{E,1}^{(\text{strain})} = \begin{pmatrix} \epsilon_{xx} - \epsilon_{yy} \\ -2\epsilon_{xy} \end{pmatrix}, \quad (\text{A14})$$

$$f_{E,2}^{(\text{strain})} = \begin{pmatrix} \epsilon_{xz} \\ \epsilon_{yz} \end{pmatrix}. \quad (\text{A15})$$

These imply $n(E) = 2$.

The symmetry-allowed spin-strain Hamiltonian is an arbitrary linear combination of the scalar products of the above-defined (1D and 2D) vectors that transform according to the same irrep. Formally, this is written in a compact fashion

as follows:

$$H_\varepsilon = \sum_{\Gamma \in \text{irreps}} \sum_{\sigma, \tau=1}^{n(\Gamma)} c_{\Gamma\sigma\tau} (f_{\Gamma\sigma}^{(\text{spin})} f_{\Gamma\tau}^{(\text{strain})}). \quad (\text{A16})$$

Here, the quantities $c_{\Gamma\sigma\tau}$ are independent real coefficients (coupling-strength parameters) that are not constrained by symmetry, and can be determined from microscopic models or experiments, as discussed in the main text. According to the counts of the previous paragraph, the sum in Eq. (A16) has eight terms, and therefore there are eight independent coupling-strength coefficients. However, since a uniform energy shift of the spin states in the Hamiltonian can be disregarded, and $f_{A_{1,1}}^{(\text{spin})}$ and $f_{A_{1,1}}^{(\text{strain})}$ do add up to a constant due to $S_x^2 + S_y^2 + S_z^2 = 2$, we can set $c_{A_{1,1,1}} = c_{A_{1,1,2}} = 0$ without the loss of generality. This implies that there are six independent nonzero coupling-strength parameters.

Direct evaluation of the terms in Eq. (A16) and comparison with Eq. (3) allows to establish the relations between the coupling-strength coefficients:

$$c_{A_{1,2,1}} = h_{41}, \quad (\text{A17a})$$

$$c_{A_{1,2,2}} = h_{43}, \quad (\text{A17b})$$

$$c_{E,1,1} = \frac{1}{4}h_{15}, \quad (\text{A17c})$$

$$c_{E,1,2} = -\frac{1}{2}h_{16}, \quad (\text{A17d})$$

$$c_{E,2,1} = -\frac{1}{4}h_{25}, \quad (\text{A17e})$$

$$c_{E,2,2} = \frac{1}{2}h_{26}. \quad (\text{A17f})$$

APPENDIX B: COMPUTING SPIN-STRAIN PARAMETERS WITH DENSITY FUNCTIONAL THEORY

We determined the spin-strain coupling-strength parameters using numerical DFT calculations. We applied DFT for electronic structure calculation combined with geometry optimization, using the PBE functional [67] in the plane-wave-based Vienna *ab initio* simulation package (VASP) [68–71]. The core electrons were treated in the projector augmented-wave (PAW) formalism [72]. The calculations were performed with 600-eV plane-wave cutoff energy. The model of the NV in bulk diamond was constructed using a 512-atom diamond simple cubic supercell within the Γ -point approximation. We use a negative sign convention for compressive strain. To model the structure subject to mechanical strain, described by the strain tensor ε , we deform the cubic supercell to a parallelepiped, whose edge vectors are obtained by transforming the undeformed edge vectors with the matrix $1 + \varepsilon$ in the cubic reference frame, and allow the atomic positions to relax. For each strain configuration, the elements of the 3×3 zero-field splitting matrix D , defining the ground-state spin Hamiltonian via $H = \mathbf{S}^T \cdot \mathbf{D} \cdot \mathbf{S}$, were calculated using the VASP implementation by Marsman with the PAW formalism [73].

We illustrate our methodology to obtain the six spin-strain coupling-strength coefficients with the example of h_{16} . To determine h_{16} , we deform the supercell using a strain tensor whose only nonvanishing element is ε_{yz} , and obtain the D matrix from the calculation. Due to Eq. (3), the chosen strain

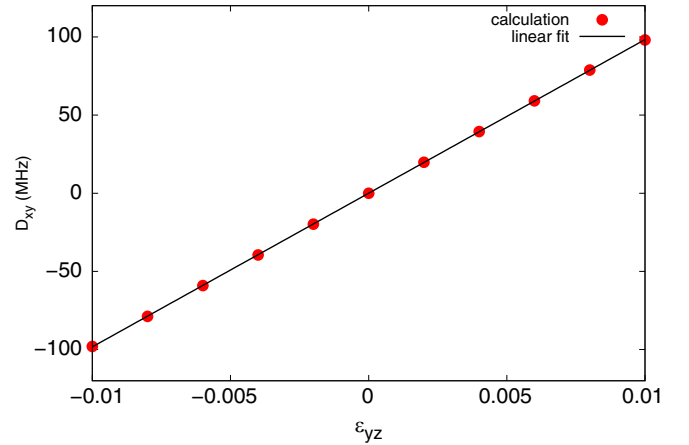


FIG. 4. Strain dependence of the zero-field splitting matrix element D_{xy} . Data points show the DFT results for the matrix element D_{xy} , as a function of the strain component ε_{xy} , with all other strain components set to zero. Solid line shows a linear fit, with a slope of 9832 ± 9 MHz/strain, allowing to obtain the coupling-strength parameter h_{16} via Eq. (B2).

configuration implies that the Hamiltonian has the form

$$H = \frac{1}{2} \varepsilon_{yz} \mathbf{S}^T \cdot \begin{pmatrix} 0 & h_{16} & 0 \\ h_{16} & 0 & h_{26} \\ 0 & h_{26} & 0 \end{pmatrix} \mathbf{S}. \quad (\text{B1})$$

This, together with the above definition of the D matrix, yields

$$h_{16} = 2 \left. \frac{\partial D_{xy}}{\partial \varepsilon_{yz}} \right|_{\varepsilon=0}. \quad (\text{B2})$$

To be able to estimate the numerical error of our DFT calculations, we infer the derivative in Eq. (B2) using a sequence of calculations with 11 equidistant values of ε_{yz} between -0.01 and 0.01 . The resulting $D_{xy}(\varepsilon_{yz})$ data points are shown in Fig. 4. From a linear fit, shown as the solid line in Fig. 4, we infer the coupling-strength coefficient h_{16} via Eq. (B2) and its standard deviation.

Similar procedures can be applied to determine the remaining five coupling-strength parameters, and the results are shown in Table I, with the following remarks. (i) To obtain the value of h_{41} and its error in Table I, we calculated the corresponding results from the ε_{xx} dependence of the D matrix, as well as from its ε_{yy} dependence, and averaged these results. (ii) We used similar averaging in the case of h_{26} and h_{16} , which we calculated from from the ε_{xz} dependence, as well as from its ε_{yz} dependence (the latter is illustrated in Fig. 4). (iii) We determined the values for h_{25} and h_{15} from the ε_{xy} dependence. In Table I, we also present the spin-stress parameters (g_{41} , etc.), which we determined from the DFT-based spin-strain parameters using the conversion procedure detailed in Appendix C.

Finally, we discuss a few observations regarding the validity of these DFT-based results. (i) To test convergence, we performed calculations with 1000-eV cutoff energy. The difference between the 600- and 1000-eV results is less than 0.6%. However, the generally used 370-eV cutoff energy in diamond is insufficient for high strain calculations, producing

nonlinear strain dependence. (ii) The 512-atom diamond supercell we used is sufficiently large for strain calculations since the main contribution to the energy splittings is caused by the strain-induced displacement of the nearest-neighbor carbon atoms of the vacancy site. The strain-induced displacements of the atoms further than the second-neighbor sites are less than 0.001 \AA in our calculations. (iii) We performed similar calculations for the hh divacancy (PL1) in 4H-SiC, where our calculated $h_{41} = 5 \text{ GHz/strain}$ coupling strength was in good order-of-magnitude agreement with the experimental ODMR shift of (2–4) GHz/strain generated by perpendicular strain [74], further supporting our calculation methodology. (iv) Our DFT calculations do not incorporate spin-orbit interaction; a quantitative description of spin-orbit effects in the presence of mechanical stress would be an important future extension. The following simple estimate based on Ref. [75] suggests that the spin-spin interaction taken into account in this work should dominate the spin-orbit contribution to the zero-field splitting matrix D . In the absence of strain, spin-orbit induces a second-order perturbative energy renormalization $h\delta D \sim \lambda^2/\Delta E$ of the zero-field splitting D , where λ is the characteristic frequency representing the spin-orbit matrix element between the ground-state triplet and a neighboring energy level, and ΔE is the energy gap between the ground-state triplet and the neighboring level. Taking [75] the nearest-neighbor level (1E), with energy gap $\Delta \sim 400 \text{ meV}$, and $\lambda/h \sim 50 \text{ GHz}$, we find $\delta D/D \approx 10^{-2}$.

APPENDIX C: CONVERTING SPIN-STRAIN PARAMETERS TO SPIN-STRESS PARAMETERS

To calculate the spin-stress coupling-strength parameters in Table I from the DFT-based spin-strain parameters, we start from the stiffness tensor C of bulk diamond, and take the following values [76] for its elements in the cubic reference frame: $C_{11} = 1076 \text{ GPa}$, $C_{12} = 125 \text{ GPa}$, $C_{44} = 576 \text{ GPa}$. First, we transform the stiffness tensor to the NV frame; we denote the resulting 6×6 stiffness matrix in the Voigt notation as C . To convert our spin-strain

Hamiltonian (3) to spin-stress Hamiltonian, we express the strain components in Eq. (3) using stress components via $\varepsilon = C^{-1}\sigma$, where $\varepsilon = (\varepsilon_{xx}, \varepsilon_{yy}, \varepsilon_{zz}, 2\varepsilon_{yz}, 2\varepsilon_{zx}, 2\varepsilon_{xy})$ and $\sigma = (\sigma_{xx}, \sigma_{yy}, \sigma_{zz}, \sigma_{yz}, \sigma_{zx}, \sigma_{xy})$ are now also in Voigt notation; note the factor of 2 in front of the off-diagonal strain components.

The inverted stiffness tensor in the NV frame reads as

$$C^{-1} = \begin{pmatrix} C_{11}^{-1} & C_{12}^{-1} & C_{13}^{-1} & 0 & C_{15}^{-1} & 0 \\ C_{12}^{-1} & C_{11}^{-1} & C_{13}^{-1} & 0 & -C_{15}^{-1} & 0 \\ C_{13}^{-1} & C_{13}^{-1} & C_{33}^{-1} & 0 & 0 & 0 \\ 0 & 0 & 0 & C_{44}^{-1} & 0 & C_{46}^{-1} \\ C_{15}^{-1} & -C_{15}^{-1} & 0 & 0 & C_{44}^{-1} & 0 \\ 0 & 0 & 0 & C_{46}^{-1} & 0 & C_{66}^{-1} \end{pmatrix}, \quad (\text{C1})$$

yielding the following following expressions for the spin-stress parameters:

$$g_{41} = h_{41}(C_{11}^{-1} + C_{12}^{-1}) + h_{43}C_{13}^{-1}, \quad (\text{C2a})$$

$$g_{43} = 2h_{41}C_{13}^{-1} + h_{43}C_{33}^{-1}, \quad (\text{C2b})$$

$$g_{26} = h_{26}\frac{1}{2}C_{44}^{-1} - h_{25}C_{15}^{-1}, \quad (\text{C2c})$$

$$g_{25} = h_{25}(C_{11}^{-1} - C_{12}^{-1}) - h_{26}C_{15}^{-1}, \quad (\text{C2d})$$

$$g_{16} = h_{16}\frac{1}{2}C_{44}^{-1} - h_{15}C_{15}^{-1}, \quad (\text{C2e})$$

$$g_{15} = h_{15}(C_{11}^{-1} - C_{12}^{-1}) - h_{16}C_{15}^{-1}. \quad (\text{C2f})$$

These relations, together with the numerical values of the inverse stiffness matrix elements,

$$C_{11}^{-1} = 86 \times 10^{-5} \text{ 1/GPa}, \quad C_{33}^{-1} = 83 \times 10^{-5} \text{ 1/GPa},$$

$$C_{44}^{-1} = 198 \times 10^{-5} \text{ 1/GPa}, \quad C_{66}^{-1} = 186 \times 10^{-5} \text{ 1/GPa},$$

$$C_{12}^{-1} = -7 \times 10^{-5} \text{ 1/GPa}, \quad C_{13}^{-1} = -4 \times 10^{-5} \text{ 1/GPa},$$

$$C_{15}^{-1} = 9 \times 10^{-5} \text{ 1/GPa}, \quad C_{46}^{-1} = -17 \times 10^{-5} \text{ 1/GPa},$$

are used to obtain the g_{41} , etc., values in Table I.

[1] L. du Preez, Ph.D. thesis, University of Witwatersrand, 1965.
[2] G. Davies and M. F. Hamer, *Proc. R. Soc. London A* **348**, 285 (1976).
[3] J. H. N. Loubser and J. P. van Wyk, *Diamond Research (London)* (Industrial Diamond Information Bureau, London, 1977), pp. 11–15.
[4] J. P. Goss, R. Jones, S. J. Breuer, P. R. Briddon, and S. Öberg, *Phys. Rev. Lett.* **77**, 3041 (1996).
[5] N. B. Manson, J. P. Harrison, and M. J. Sellars, *Phys. Rev. B* **74**, 104303 (2006).
[6] A. Gali, M. Fyta, and E. Kaxiras, *Phys. Rev. B* **77**, 155206 (2008).
[7] F. Jelezko, T. Gaebel, I. Popa, A. Gruber, and J. Wrachtrup, *Phys. Rev. Lett.* **92**, 076401 (2004).
[8] A. Gruber, A. Dräbenstedt, C. Tietz, L. Fleury, J. Wrachtrup, and C. von Borczyskowski, *Science* **276**, 2012 (1997).

[9] G. Balasubramanian, P. Neumann, D. Twitchen, M. Markham, R. Kolesov, N. Mizuochi, J. Isoya, J. Achard, J. Beck, J. Tissler, V. Jacques, P. R. Hemmer, F. Jelezko, and J. Wrachtrup, *Nat. Mater.* **8**, 383 (2009).
[10] H. Bernien, B. Hensen, W. Pfaff, G. Koolstra, M. S. Blok, L. Robledo, T. H. Taminiau, M. Markham, D. J. Twitchen, L. Childress, and R. Hanson, *Nature (London)* **497**, 86 (2013).
[11] B. Hensen, H. Bernien, A. E. Dréau, A. Reiserer, N. Kalb, M. S. Blok, J. Ruitenbergh, R. F. L. Vermeulen, R. N. Schouten, C. Abellán, W. Amaya, V. Pruneri, M. W. Mitchell, M. Markham, D. J. Twitchen, D. Elkouss, S. Wehner, T. H. Taminiau, and R. Hanson, *Nature (London)* **526**, 682 (2015).
[12] N. Kalb, A. A. Reiserer, P. C. Humphreys, J. J. W. Bakermans, S. J. Kamerling, N. H. Nickerson, S. C. Benjamin, D. J. Twitchen, M. Markham, and R. Hanson, *Science* **356**, 928 (2017).

- [13] G. Balasubramanian, I. Y. Chan, R. Kolesov, M. Al-Hmoud, J. Tisler, C. Shin, C. Kim, A. Wojcik, P. R. Hemmer, A. Krueger, T. Hanke, A. Leitenstorfer, R. Bratschitsch, F. Jelezko, and J. Wrachtrup, *Nature (London)* **455**, 648 (2008).
- [14] J. R. Maze, P. L. Stanwix, J. S. Hodges, S. Hong, J. M. Taylor, P. Cappellaro, L. Jiang, M. V. G. Dutt, E. Togan, A. S. Zibrov, A. Yacoby, R. L. Walsworth, and M. D. Lukin, *Nature (London)* **455**, 644 (2008).
- [15] F. Dolde, H. Fedder, M. W. Doherty, T. Nöbauer, F. Rempp, G. Balasubramanian, T. Wolf, F. Reinhard, L. C. L. Hollenberg, F. Jelezko, and J. Wrachtrup, *Nat. Phys.* **7**, 459 (2011).
- [16] D. M. Toyli, C. F. d. I. Casas, D. J. Christle, V. V. Dobrovitski, and D. D. Awschalom, *Proc. Natl. Acad. Sci. USA* **110**, 8417 (2013).
- [17] P. Neumann, I. Jakobi, F. Dolde, C. Burk, R. Reuter, G. Waldherr, J. Honert, T. Wolf, A. Brunner, J. H. Shim, D. Suter, H. Sumiya, J. Isoya, and J. Wrachtrup, *Nano Lett.* **13**, 2738 (2013).
- [18] G. Kucsko, P. C. Maurer, N. Y. Yao, M. Kubo, H. J. Noh, P. K. Lo, H. Park, and M. D. Lukin, *Nature (London)* **500**, 54 (2013).
- [19] J. Teissier, A. Barfuss, P. Appel, E. Neu, and P. Maletinsky, *Phys. Rev. Lett.* **113**, 020503 (2014).
- [20] A. Barfuss, J. Teissier, E. Neu, A. Nunnenkamp, and P. Maletinsky, *Nat. Phys.* **11**, 820 (2015).
- [21] P. Ovarthaiyapong, K. W. Lee, B. A. Myers, and A. C. B. Jayich, *Nat. Commun.* **5**, 4429 (2014).
- [22] J. Cramer, N. Kalb, M. A. Rol, B. Hensen, M. S. Blok, M. Markham, D. J. Twitchen, R. Hanson, and T. H. Taminiau, *Nat. Commun.* **7**, 11526 (2016).
- [23] G. Waldherr, Y. Wang, S. Zaiser, M. Jamali, T. Schulte-Herbruggen, H. Abe, T. Ohshima, J. Isoya, J. F. Du, P. Neumann, and J. Wrachtrup, *Nature (London)* **506**, 204 (2014).
- [24] T. H. Taminiau, J. Cramer, T. van der Sar, V. V. Dobrovitski, and R. Hanson, *Nat. Nanotechnol.* **9**, 171 (2014).
- [25] J. R. Maze, A. Gali, E. Togan, Y. Chu, A. Trifonov, E. Kaxiras, and M. D. Lukin, *New J. Phys.* **13**, 025025 (2011).
- [26] M. W. Doherty, N. B. Manson, P. Delaney, and L. C. L. Hollenberg, *New J. Phys.* **13**, 025019 (2011).
- [27] M. W. Doherty, F. Dolde, H. Fedder, F. Jelezko, J. Wrachtrup, N. B. Manson, and L. C. L. Hollenberg, *Phys. Rev. B* **85**, 205203 (2012).
- [28] M. W. Doherty, N. B. Manson, P. Delaney, F. Jelezko, J. Wrachtrup, and L. C. Hollenberg, *Phys. Rep.* **528**, 1 (2013).
- [29] J. Cai, F. Jelezko, and M. B. Plenio, *Nat. Commun.* **5**, 4065 (2014).
- [30] E. R. MacQuarrie, T. A. Gosavi, A. M. Moehle, N. R. Jungwirth, S. A. Bhave, and G. D. Fuchs, *Optica* **2**, 233 (2015).
- [31] E. R. MacQuarrie, T. A. Gosavi, N. R. Jungwirth, S. A. Bhave, and G. D. Fuchs, *Phys. Rev. Lett.* **111**, 227602 (2013).
- [32] E. R. MacQuarrie, M. Otten, S. K. Gray, and G. D. Fuchs, *Nat. Commun.* **8**, 14358 (2017).
- [33] E. R. MacQuarrie, T. A. Gosavi, S. A. Bhave, and G. D. Fuchs, *Phys. Rev. B* **92**, 224419 (2015).
- [34] M. S. J. Barson, P. Peddibhotla, P. Ovarthaiyapong, K. Ganesan, R. L. Taylor, M. Gebert, Z. Mielens, B. Koslowski, D. A. Simpson, L. P. McGuinness, J. McCallum, S. Praver, S. Onoda, T. Ohshima, A. C. Bleszynski Jayich, F. Jelezko, N. B. Manson, and M. W. Doherty, *Nano Lett.* **17**, 1496 (2017).
- [35] D. A. Golter, T. Oo, M. Amezcua, K. A. Stewart, and H. Wang, *Phys. Rev. Lett.* **116**, 143602 (2016).
- [36] D. A. Golter, T. Oo, M. Amezcua, I. Lekavicius, K. A. Stewart, and H. Wang, *Phys. Rev. X* **6**, 041060 (2016).
- [37] S. Meesala, Y.-I. Sohn, H. A. Atikian, S. Kim, M. J. Burek, J. T. Choy, and M. Lončar, *Phys. Rev. Appl.* **5**, 034010 (2016).
- [38] E. van Oort and M. Glasbeek, *Chem. Phys. Lett.* **168**, 529 (1990).
- [39] M. Matsumoto, K. Chimata, and M. Koga, *J. Phys. Soc. Jpn.* **86**, 034704 (2017).
- [40] Y. Kato, R. C. Myers, A. C. Gossard, and D. D. Awschalom, *Nature (London)* **427**, 50 (2004).
- [41] K. C. Nowack, F. H. L. Koppens, Y. V. Nazarov, and L. M. K. Vandersypen, *Science* **318**, 1430 (2007).
- [42] V. N. Golovach, M. Borhani, and D. Loss, *Phys. Rev. B* **74**, 165319 (2006).
- [43] P. V. Klimov, A. L. Falk, B. B. Buckley, and D. D. Awschalom, *Phys. Rev. Lett.* **112**, 087601 (2014).
- [44] A. Norambuena, E. Muñoz, H. T. Dinani, A. Jarmola, P. Maletinsky, D. Budker, and J. R. Maze, *Phys. Rev. B* **97**, 094304 (2018).
- [45] D. A. Broadway, J. D. A. Wood, L. T. Hall, A. Stacey, M. Markham, D. A. Simpson, J.-P. Tetienne, and L. C. L. Hollenberg, *Phys. Rev. Appl.* **6**, 064001 (2016).
- [46] V. Jacques, P. Neumann, J. Beck, M. Markham, D. Twitchen, J. Meijer, F. Kaiser, G. Balasubramanian, F. Jelezko, and J. Wrachtrup, *Phys. Rev. Lett.* **102**, 057403 (2009).
- [47] V. Ivády, P. V. Klimov, K. C. Miao, A. L. Falk, D. J. Christle, K. Szász, I. A. Abrikosov, D. D. Awschalom, and A. Gali, *Phys. Rev. Lett.* **117**, 220503 (2016).
- [48] B. Smeltzer, J. McIntyre, and L. Childress, *Phys. Rev. A* **80**, 050302 (2009).
- [49] M. Steiner, P. Neumann, J. Beck, F. Jelezko, and J. Wrachtrup, *Phys. Rev. B* **81**, 035205 (2010).
- [50] M. Chen, M. Hirose, and P. Cappellaro, *Phys. Rev. B* **92**, 020101 (2015).
- [51] S. Felton, A. M. Edmonds, M. E. Newton, P. M. Martineau, D. Fisher, D. J. Twitchen, and J. M. Baker, *Phys. Rev. B* **79**, 075203 (2009).
- [52] F. Jelezko, T. Gaebel, I. Popa, M. Domhan, A. Gruber, and J. Wrachtrup, *Phys. Rev. Lett.* **93**, 130501 (2004).
- [53] G. D. Fuchs, V. V. Dobrovitski, D. M. Toyli, F. J. Heremans, and D. D. Awschalom, *Science* **326**, 1520 (2009).
- [54] M. J. A. Schuetz, E. M. Kessler, G. Giedke, L. M. K. Vandersypen, M. D. Lukin, and J. I. Cirac, *Phys. Rev. X* **5**, 031031 (2015).
- [55] A. Crippa, R. Maurand, L. Bourdet, D. Kotekar-Patil, A. Amisse, X. Jehl, M. Sanquer, R. Laviéville, H. Bohuslavskiy, L. Hutin, S. Barraud, M. Vinet, Y.-M. Niquet, and S. De Franceschi, *Phys. Rev. Lett.* **120**, 137702 (2018).
- [56] G. D. Fuchs, G. Burkard, P. V. Klimov, and D. D. Awschalom, *Nat. Phys.* **7**, 789 (2011).
- [57] L. Childress, M. V. Gurudev Dutt, J. M. Taylor, A. S. Zibrov, F. Jelezko, J. Wrachtrup, P. R. Hemmer, and M. D. Lukin, *Science* **314**, 281 (2006).
- [58] L. Robledo, L. Childress, H. Bernien, B. Hensen, P. F. A. Alkemade, and R. Hanson, *Nature (London)* **477**, 574 (2011).
- [59] M. Ogura and H. Akai, *Appl. Phys. Lett.* **91**, 253118 (2007).
- [60] S. Thiele, F. Balestro, R. Ballou, S. Klyatskaya, M. Ruben, and W. Wernsdorfer, *Science* **344**, 1135 (2014).
- [61] A. J. Sigillito, A. M. Tyryshkin, T. Schenkel, A. A. Houck, and S. A. Lyon, *Nat. Nanotechnol.* **12**, 958 (2017).

- [62] G. Tosi, F. A. Mohiyaddin, S. Tenberg, A. Laucht, and A. Morello, Robust electric dipole transition at microwave frequencies for nuclear spin qubits in silicon, [arXiv:1706.08095](https://arxiv.org/abs/1706.08095).
- [63] P. Boross, G. Széchenyi, and A. Pályi, *Phys. Rev. B* **97**, 245417 (2018).
- [64] J. Mansir, P. Conti, Z. Zeng, J. J. Pla, P. Bertet, M. W. Swift, C. G. Van de Walle, M. L. W. Thewalt, B. Sklenard, Y. M. Niquet, and J. J. L. Morton, *Phys. Rev. Lett.* **120**, 167701 (2018).
- [65] C. P. Slichter, *Principles of Magnetic Resonance* (Harper & Row, New York, 1963).
- [66] S. Sangtawesin, C. A. McLellan, B. A. Myers, A. C. B. Jayich, D. D. Awschalom, and J. R. Petta, *New J. Phys.* **18**, 083016 (2016).
- [67] J. P. Perdew, K. Burke, and M. Ernzerhof, *Phys. Rev. Lett.* **77**, 3865 (1996).
- [68] G. Kresse and J. Hafner, *Phys. Rev. B* **47**, 558 (1993).
- [69] G. Kresse and J. Furthmüller, *Phys. Rev. B* **54**, 11169 (1996).
- [70] G. Kresse and J. Furthmüller, *Comput. Mater. Sci.* **6**, 15 (1996).
- [71] J. Paier, M. Marsman, K. Hummer, G. Kresse, I. C. Gerber, and J. G. Ángyán, *J. Chem. Phys.* **124**, 154709 (2006).
- [72] P. E. Blöchl, *Phys. Rev. B* **50**, 17953 (1994).
- [73] Z. Bodrog and A. Gali, *J. Phys.: Condens. Matter* **26**, 015305 (2014).
- [74] A. L. Falk, P. V. Klimov, B. B. Buckley, V. Ivády, I. A. Abrikosov, G. Calusine, W. F. Koehl, A. Gali, and D. D. Awschalom, *Phys. Rev. Lett.* **112**, 187601 (2014).
- [75] G. Thiering and A. Gali, *Phys. Rev. B* **96**, 081115 (2017).
- [76] E. Kaxiras, *Atomic and Electronic Structure of Solids* (Cambridge University Press, Cambridge, 2003).